Subradiant dipolar interactions in plasmonic nanoring resonator array for integrated label-free biosensing

Yuzhang Liang[1], Hui Zhang[1], Wenqi Zhu[2,3], Amit Agrawal[2,3], Henri Lezec[2], Lixia Li[4], Wei Peng[4], Yi Zou[1], Yanqing Lu[1,*] and Ting Xu[1,*]

[1] National Laboratory of Solid State Microstructures, College of Engineering and Applied Sciences, Collaborative Innovation Center of Advanced Microstructures, Nanjing University, Nanjing 210093, China.

[2] Center for Nanoscale Science and Technology, National Institute of Standards and Technology, Gaithersburg, MD 20899, USA.

[3] Maryland NanoCenter, University of Maryland, College Park, MD 20742, USA.

[4] College of Physics and Optoelectronics Engineering, Dalian University of Technology, Dalian 116024, China.

Abstract

With the development of advanced nanofabrication technologies over the last decade, plasmonic nanostructures have attracted wide attention for their potential in label-free biosensing applications. However, the sensing performance of nanostructured plasmonic sensors is primarily limited by the broad-linewidth features with low peak-to-dip signal ratio in the extinction spectra that result from strong radiative damping. Here, we propose and systematically investigate the in-plane and out-of-plane dipolar interactions in an array of plasmonic nanoring resonators that are from the spatial combination of classic nanohole and nanodisk structures. Originating from the strong coupling of the dipolar modes from parent nanohole and nanodisk structures, the subradiant lattice plasmon resonance in the nanoring

resonator array exhibits narrow-linewidth spectral features with high peak-to-dip signal ratio and strong near-field electromagnetic enhancement, making it an ideal platform for high-sensitivity chemical and bio-medical sensing. We experimentally demonstrate that the plasmonic nanoring resonator array can be used for high-sensitivity refractive index sensing and real-time monitoring of biomolecular specific binding interactions at nanomolar concentration. Moreover, thanks to its simple normal incident illumination scheme and polarization independent optical response, we further transfer the plasmonic nanoring resonator array onto the optical fiber tip to demonstrate an integrated and miniaturized platform for label-free remote biosensing, which implies that the plasmonic nanoring resonator array may be a potential candidate for developing high performance and highly-integrated photonic biosensing systems.

Keywords: Plasmonic nanostructure, Biosensing, Dipolar Interaction, Fiber Optics, Protein binding, Point of care diagnostics

Localized surface plasmon resonance (LSPR) in a variety of plasmonic nanostructures, such as discrete metallic nanodisks and nanoparticles, have received significant attention for their potential in low-cost, label-free biosensors.[1-21] In contrast to the conventional propagating surface plasmon based sensors relying on bulky prism-coupling mechanism,[22-24] the size of nanostructured LSPR sensors can be shrunk to the micrometer scale. This makes them very attractive for the design of portable devices for point-of-care testing (POCT) application.[25] In contrast to the centralization and increased efficiency in laboratory diagnostics, POCT shortens the time of transport and preparation of clinical samples and biochemical-test results are rapidly available at the point of care. But unfortunately, the sensing performance of LSPR sensor is always limited by the broad-linewidth features with low peak-to-dip signal ratio in the extinction spectra resulting from strong radiative damping, which significantly limits the intensity of localized electromagnetic fields around the isolated nanostructures.[26,27] Hence, the quest to suppress the radiative damping is essential in the research field of plasmonic biosensing. Recent works have suggested that by carefully engineering plasmonic nanostructures, such as concentric nanocavity[28-30] and closely packed nanoparticle cluster,[31-34] higher localized electromagnetic fields and narrower line-shape can be achieved for subradiant plasmon resonance, which in principle can be used to improve the sensing performance.

Another effective approach to manipulate plasmon linewidth spectral features of nanostructures is to assemble them into an array. Because optical energy scattered by one nanostructure unit cell will be captured by neighboring nanostructure as plasmon instead of decaying as free-space propagating light, the array exhibits completely different optical

responses from those of an isolated nanostructure. Recently, it has been demonstrated that strongly coupled one- and two-dimensional nanostructure arrays can produce narrow lattice plasmon resonance by suppressing radiative losses.[35-38] Therefore, nanostructure arrays supporting subradiant lattice plasmon resonance have emerged as a powerful photonic platform for sensing applications.

Here, we develop a novel, high-sensitivity label-free biosensing platform based on a plasmonic nanoring resonator array (PNRA), which is constructed from the spatial combination of nanohole and nanodisk arrays. Based on coupled dipole theory, the in-plane and out-of-plane strong coupling of the dipolar modes from parent nanohole and nanodisk structures in PNRA generates a sharp subradiant lattice plasmon resonance with an extremely narrow linewidth (~7 nm), a high peak-to-dip signal ratio (0.7), and high refractive index sensitivity (~545 nm·RIU^{-1}). The PNRA device are utilized here to experimentally achieve high sensitivity microfluidic refractive index sensing and real-time monitoring of biomolecular interaction between Ribonuclease B (RNase B) and Concanavalin A (Con A) protein molecules at ultralow concentrations. Importantly, compared to previous works that uses complicated angular illuminations and specific polarizations to excite high-order guide modes in metamaterials[39-40] or optical Fano resonances in nanostructures for sensing,[41-43] the subradiant fundamental lattice plasmon resonance in PNRA can be excited by using normally incident randomly polarized light and generate a stable spectral line-shape with a high peak-to-dip signal ratio around the resonant wavelength. This implies that our device is able to be conveniently probed where the incident and reflected light are efficiently collected by the same optical path. As a proof-of-concept demonstration, we successfully transfer the PNRA onto the tip of an optical

fiber for further miniaturization and integration. The sensing performance of optical fiber sensor with PNRA confirms it as a robust tool for remotely detecting biomolecules interaction.[44-47]

Results

Fabrication and characterization of PNRA

The schematic diagram of the designed PNRA biosensor is depicted in **Figure 1a.** The structure can be regarded as the spatial combination of simple nanohole and nanodisk arrays arranged in a hexagonal lattice, where the gap between nanohole and nanodisk forms nanoring. Due to the axial symmetry of the structure, the optical properties of PNRA are independent on the polarization direction of the normally incident light. The reflectance spectrum of the structure is investigated using full-wave simulation based on the finite-difference time-domain (FDTD) algorithm. The structural parameters are as follows: periodicity P = 640 nm, inner radius r = 150 nm, outer radius D = 240 nm and the thickness of Au film is 100 nm. The top surface of the PNRA is covered with a medium having a refractive index (RI) of 1.331 to match that of the aqueous solution in experiment. The calculated reflectance spectrum is plotted in **Figure 1b** (blue solid line), where the two resonance dips can be observed at wavelengths of λ_1 = 758 nm and λ_2 = 838 nm. The reflectance dip at λ_1 has a full-width at half-maximum (FWHM) linewidth of ~7 nm, which results in a quality factor (Q-factor) that reaches ~108. The reflectance dip at λ_2 has ~14 nm FWHM and ~ 60 Q-factor (see Methods for details on the extraction of FWHM and Q-factor).

Inset of **Figure 1a** shows the top-down scanning electron microscopy (SEM) image of the fabricated sample. Before the optical measurements, the top surface of the PNRA is immersed in an aqueous solution with a Polydimethylsiloxane (PDMS) flow cell. The fabricated structure

is illuminated with a randomly polarized normally incident white light from the substrate side. The experimentally measured reflectance spectrum is depicted in **Figure 1b** (red solid line), where two resonance dips are also observed at the wavelengths of 750 nm and 838 nm. The measured FWHM and *Q*-factor of the resonance dip at λ_1 (λ_2) are ~15 nm (~40 nm) and ~50 (~21), respectively. The relative wider FWHM and lower *Q*-factors achieved in experiment can be attributed to three factors: First, surface roughness of fabricated structure is limited by the grain sizes of multi-crystalline gold film produced by vacuum coating, which introduces scattering losses; Second, the geometry parameters of the fabricated sample in experiment are slightly different from those of simulated model. For example, outer radius (*D*) of nanoring array in experiment may be larger than that of numerical simulation. As shown in Supplementary **Figure S1a**, we theoretically find that the line-shape of resonant wavelength λ_1 becomes wider with the increase of outer radius; Third, an objective lens with a numerical aperture (NA) of 0.10 is used for the spectral measurements. A non-zero NA objective results in sample excitation at oblique incidence angles, which decreases the spatial coherence among different modes and generates a wide spectral line-shape in experiment.[48,49] The simulated and measured reflectance spectra for different outer radius of nanoring and using different numerical aperture of objective are shown in Supplementary **Figure S1b**. Nevertheless, both the spectral line-shape and the position of the resonance dips measured in experiment are in good agreement with those calculated using FDTD simulation. **Figures 1c and 1d** depicts electric field distribution on the top and bottom surfaces of nanoring array at resonant wavelengths λ_1 and λ_2, respectively. For resonance wavelength λ_1, electric field is mainly localized on top surface of the PNRA structure. However, electric field is mainly localized at

the bottom surface for resonance wavelength λ_2. This indicates that two dip of reflectance spectrum not only is frequency separation, but also the spatial localization of optical energy is also separated. These characteristics make the PNRA structure very useful for the design of plasmonic sensors.

Theoretical analysis of dipolar interactions in PNRA

The calculated reflectance (absorptance) spectrum of the PNRA exhibits two resonance dips (peaks) at λ_1 = 758 nm and λ_2 = 838 nm, as shown in **Figure 2a**. These two resonance dips can be qualitatively explained by using plasmonic hybridization theory.[50-53] To further understand these resonances in detail, we first calculate the in-plane normalized surface charge distributions of the relevant modes at both top and bottom surfaces of nanoring, nanhole and nanodisk arrays at resonant wavelengths λ_1 and λ_2 (**Figure 2b-2d**). As expected, the mode distributions of PNRA are exactly the spatial superposition of the in-plane dipolar modes respectively from nanohole and nanodisk structures. At resonant wavelength λ_1, dipolar modes at the top surfaces of nanohole and nanodisk structures have opposite orientations. The anti-parallel dipolar interaction reduces the total dipole momentum and minimizes the radiative damping of the PNRA system, which is a typical subradiant characterization. [28,29] As a result, anti-parallel dipolar at the top surface can effectively trap the incident light and excite subradiant lattice plasmon resonance, resulting in a large narrow-linewidth absorptance peak at λ_1. On the other side, in-plane dipolar modes at the bottom surfaces of nanohole and nanodisk structures are oriented in the same direction at λ_1. The parallel dipolar interaction enhances the total dipole momentum and results in a rapid depletion of the plasmon energy. Compared with the top surface, the optical intensity at the bottom surface of a PNRA is much weaker (**Figure**

1c). Therefore, enhanced optical field at top surface for resonance wavelength λ_1 is sensitive to the change of ambient environment, which can be used for sensing application.

Contrary to λ_1, the dipolar interactions at resonant wavelength λ_2 are opposite: parallel dipolar interactions occur at the top surface while anti-parallel dipolar interactions occur at the bottom surface. Therefore, the optical energy is mainly localized at the bottom surface of PNRA at the wavelength of 838 nm (**Figure 1d**). Because the bottom surface of PNRA is glass substrate and not in contact with the microfluidics, the plasmon resonance at λ_2 cannot be used for sensing applications. Moreover, the optical field at the top surface for resonance wavelength λ_2 is immune to the ambient environment, which can serve as a self-reference channel for sensing detection.

Besides investigating the in-plane dipolar interactions, we also calculate the out-of-plane normalized surface charge distributions of PNRA at resonant wavelengths λ_1 and λ_2, as shown in **Figure 2e**. It can be clearly seen that at the resonant wavelengths, the normalized surface charge distributions respectively form an out-of-plane dipolar (quadrupolar) mode for the parent nanohole (nanodisk) structure. The out-of-plane quadrupolar mode in nanodisk array originates from the geometry-dependent dipolar interaction between large nanoparticle structures arranged in a two-dimensional array.[38] Due to the interference between out-of-plane dipolar and quadrupolar modes, the PNRA exhibits a Fano-like asymmetric peak-and-dip spectral profile at resonance and strongly localizes the optical field around the structure. As shown in **Figure S2**, the absorption and optical field intensity at the top surface of the PNRA are much stronger than those of pure nanohole and nanodisk structures at the resonant wavelengths, which is beneficial for sensing applications. This optical field primarily overlaps

with the volume containing the material to be sensed, satisfying an important criterion for development of a plasmonic sensor with high figure-of-merit (FOM).

Sensing performance of the PNRA

To examine the real-time sensing performance of the PNRA as a refractive index sensor, a microchannel-based miniaturized biosensor platform is fabricated by assembling a microfluidic system on the top of PNRA. To calibrate and determine the detection limit of the sensor, sodium chloride (NaCl) solutions with refractive indices (RIs) of 1.3310, 1.3420, 1.3512, 1.3596, 1.3688, and 1.3780 are manually injected into the flow channel using a peristaltic pump at a constant flow rate of 0.2 ml/min. The RIs of the sodium chloride solutions are calibrated using an Abbe refractometer. The measured reflectance spectra of the PNRA coated with NaCl solutions of different RIs are shown in **Figure 3a**. As the RI of the injected solution increases, a red shift of the resonance dip around the wavelength of 750 nm occurs. For the second resonance dip around the wavelength of 838 nm, because the optical intensity localized at bottom surface is non-contact with NaCl solutions, no variation in the measured spectrum is observed. Within the investigated RI range, the line-shape of the fundamental lattice plasmon resonance does not vary and keeps a very high peak-to-dip signal ratio, indicating a stable operation of the sensing device. The FDTD calculated reflectance spectra for an equivalent change in bulk refractive index of the media surrounding that PNRA are shown in Supplementary **Figure S3a**. The calculated spectral resonance line-shape and its location exhibit good agreement with the experimental results. The peak-to-dip signal contrast around the resonant wavelength, *SC*, define as $SC = R_{peak}-R_{dip}$, is an important parameter associated with the signal-to-noise ratio of the sensing devices. Compared to that of nanohole

and nanodisk structures (Supplementary **Figure S4**), the *SC* of the PNRA structure (~0.7) is higher in simulation and experiment thanks to the highly localized optical fields caused by the subradiant dipolar interactions. This value is several times higher than that of other nanostructured plasmonic sensors[9-10, 29, 31, 35, 38] and will be beneficial for easily detecting and distinguishing the sensing signal from background noise.

Besides peak-to-dip signal ratio, we also analyze another three critical parameters: RI sensitivity, figure of merit (FOM), and limit of detection (LOD) to quantitatively evaluate the sensing performance of the device. RI sensitivity, S, is defined as the resonance wavelength shift, $\Delta\lambda$, for a change in the bulk RI, Δn (*i.e.*, $S = \Delta\lambda/\Delta n$). The spectral-dip location in the reflectance spectra as a function of RI is plotted in **Figure 3b**. A RI sensitivity of 513 nm·RIU^{-1} is obtained by calculating the slope of the linear-fit to the experimental results, which agrees well with the calculated sensitivity of (545 nm·RIU^{-1} as shown in Supplementary **Figure S3b**. Furthermore, we respectively calculates the influence of structure parameters of nanoring array (including periodicity P, inner radius r and out radius R) on resonant wavelength λ_1 and RI sensitivity. The results have been plotted in Supplementary **Figure S5**. These results indicates both resonant wavelength λ_1 and RI sensitivity increases linearly with increased periodicity. In order to achieve the sensing detection of PNRA structure at the visible frequency, the periodicity P = 640 nm is selected in the paper. With fixed structure periodicity, optimized RI sensitivity can be obtained by selecting appropriate the size of inner and outer radii. In addition, the change of inner and outer radii could also significantly influence the peak-to-dip signal ratio at the resonant wavelength λ_1. FOM, defined as FOM = $S/(2\gamma)$ (the sign 2γ refers to the FWHM of the resonance dip obtained in the Q-factor extraction), is a widely accepted metric

that determines the sensitivity performance of an optical sensor, and is inversely proportional to the spectral sharpness of resonance. Experimentally measured FOM value is ~35 RIU^{-1} (Supplementary **Figure S6**), which is several times higher than the FOM achieved with nanoparticle-based plasmonic sensors.[4-7, 32, 43] The FDTD calculated FOM value of ~78 RIU^{-1} is a factor of two higher than the experimentally measured values due to a wider $\Delta\lambda$ obtained in experiment. In principle, the experimental FOM can be further improved by optimizing nanofabrication techniques to achieve smaller metal scattering losses, or by using a lower NA objective lens in the measurement.

In addition to the RI sensitivity and FOM, LOD is also a key parameter for characterizing the performance of a sensing device. The LOD is defined as LOD = $N/S = \Delta n/(\Delta\lambda/N)$, where S is RI sensitivity and N refers to the experimental spectral noise. In our experiment, N is obtained by calculating the standard deviation of the experimental signal for a duration of 80 minutes with a time resolution of 5 s. **Figure 3c** shows the real-time response of the resonance dip for NaCl solution with different RI. Using the measured data shown in **Figure 3c**, the experiment noise N for different RI solutions is 0.0674 nm, 0.0608 nm, 0.0718 nm, 0.0714 nm, 0.0628 nm, and 0.0656 nm, respectively. Therefore, based on the relationship between the signal-to-noise ratio ($\Delta\lambda/N$) and the change of RI shown in **Figure 3d**, we can achieve a LOD of ~1.3219×10^{-4} RIU for our sensor device. This LOD value is comparable to that of the previously reported SPR sensor based on prism-coupling configuration.[54]

Real-time detection of specific binding between protein molecules

To further demonstrate the ability of PNRA as high-performance biosensor, we perform the experiments to detect in real-time the specific binding of RNase B and Con A protein

molecules in solution on the sensing surface. The specific binding of RNase B and Con A has been extensively studied as a standard affinity model for biosensors.[55-56] To capture the Con A biomolecule at different concentrations, the fabricated PNRA sensor is functionalized with immobilized RNase B. The immobilization process of RNase B is depicted in **Figure 4a**. First, the sensing chip is cleaned with ultrapure water and ethanol. After a subsequent wash, the sensing substrate is dipped into an ethanol solution of 11-mercaptoundecanoic acid (MUA, 10 mM) at room temperature for 24 hours to self-assemble an alkanethiol monolayer on the surface of gold layer. The unreacted thiol molecules are washed away by using ethanol. After drying under N_2 gas, a mixed aqueous solution containing 1-ethyl-3-(3-dimethylamino-propyl) carbodiimide hydrochloride (EDC, 0.55 M) and N-hydroxysuccinimide (NHS, 0.5 M) is used for 30 minutes at 4 °C to activate the alkanethiol monolayer on the gold surface. Then, the sensing chip is rinsed with deionized water and dried under N_2 gas. After activating, the sensing chip is equipped with the microfluidic channel. The growth process of biomolecules on the surface of structure is dynamically monitored in real-time. 0.1 mg/ml RNase B in phosphate buffered saline (PBS) is injected into the sensor microchannel for 30 minutes to form stable monomolecular layer. After the rinsing in PBS buffer, bovine serum albumin (BSA, 0.1 mg/ml) is used for 30 minutes to deactivate the remaining activated carboxyl sites that did not combine with the RNase B.

Different concentrations of Con A ranging from 0.02 mg/ml to 0.20 mg/ml are monitored by regenerating the biosensor surface. **Figure 4b** shows the wavelength changes of resonance dip λ_1 with a time resolution of 5 s to dynamically monitor the specific binding between RNase B and Con A. The monitoring process is depicted as follows: First, PBS solution is injected

into flow channel to obtain the baseline. Then, Con A solution is pumped to bind with RNase B on the sensing surface. Next, PBS buffer solution removes the unbound Con A molecules. Finally, the 0.8 mol/L urea solution is used to strip the surface-bound Con A molecules to effectively regenerate the sensing region, and the next concentration can be tested sequentially. As shown in **Figure 4b**, the baseline of our sensor chip is very stable during the measurement. Abrupt changes of the resonance wavelength after injecting Con A are observed in the sensing curves, which is attributed to the occurrence of specific binding between Con A and RNase B. The association and dissociation rate between Con A and RNase B is also calculated based on sensing curves in **Figure 4b**. As a contrast, the non-specific binding between anti-IgG and RNase B does not result in the red shift of resonance wavelength, which illustrate specific binding between Con A and RNase B. To validate reliability and repeatability, each concentration of Con A is measured three times using the same senor chip. The experiment results are summarized in **Figure 4c**. Determined from the experimental noise and the relationship between the wavelength response and Con A concentration, the detection limit for Con A is estimated to be 4.6 μg/ml (45 nM), which indicates that the PNRA offers a high performance photonic platform for label-free biomolecular detection.

The PNRA integrated on the optical fiber for label-free remote biosensing

As we analyzed above, the subradiant dipolar interactions and lattice plasmon resonance can be excited by the normally incident randomly polarized light. Therefore, the PNRA structure is able to be transferred onto the tip of optical fiber for further integration and miniaturization. Herein we demonstrate an optical fiber biosensor by integrating the PNRA on the fiber tip as a remote biosensing platform. The schematic diagram of the designed optical

fiber biosensor is depicted in **Figure 5a**. The structural parameters of PNRA on the fiber tip are identical to that on the quartz substrate. The designed optical fiber biosensor is fabricated by sequentially depositing 3 nm thick Ti layer and 100 nm thick Au film on the fine polishing end face of a 20-cm long optical fiber (the specification of fiber: core/cladding/coating, 200/220/270 μm; NA~ 0.22). The PNRA is patterned using FIB over a 150 μm × 150 μm area. **Figure 5b** shows SEM and microscope images of the fabricated sample.

To evaluate the sensing performance of optical fiber sensor integrated with PNRA, a home-made flow cell is assembled on the fiber tip. The measured reflectance spectra for the NaCl solutions with different RIs are shown in **Figure 5c**. The RIs and flow rate of NaCl solutions for the measurement using the optical fiber sensor are identical to that of quartz substrate device. It can be clearly seen that resonance dip around the wavelength of 755 nm has an obvious red shift and resonance dip around 850 nm does not vary with the increase of RIs of NaCl solutions. Compared to that of PNRA on the quartz substrate, the line-shape of resonance dip broadens for the PNRA on the fiber tip because the fiber used in experiment has a larger NA. The spectral-dip location around the wavelength of 755 nm as a function of RI is depicted in **Figure 5d**. A RI sensitivity of around 520 nm·RIU^{-1} is obtained for optical fiber sensor, which matches well with that of quartz substrate device.

Finally, to determine the capability of our designed optical fiber sensor for dynamic monitoring biomolecule interactions, we perform the same experiment to detect in real-time the specific binding of RNase B and Con A protein molecules in solution on the sensing surface. **Figure 5e** shows the wavelength changes of resonance dip with a time resolution of 1 s to dynamically monitor the specific binding between RNase B and Con A. Similarly, each

concentration of Con A is measured three times using our optical fiber sensor to validate reliability and repeatability. As summarized in **Figure 5f**, the experiment results imply that the detection limit of optical fiber sensor for Con A is about 6.0 μg/ml (59 nM), very similar to the quartz substrate device. These results confirm that the PNRA offers a high performance photonic platform for the design of miniaturized biosensor for point-of-care and remote biosensing.

Discussion and conclusion

The designed PNRA sensor has a wide RI detection range. As shown in the Supplementary **Figure S7a**, we theoretically investigate the reflectance spectra of the PNRA with the RI range from 1.33 to 1.55. Resonance dip λ_1 always keep narrow line-shape and high peak-to-dip signal ratio within the investigated RI range expect the specific point where there are an intersection between resonance wavelengths λ_1 and λ_2. The PNRA sensor exhibits a good linearity between resonance wavelength λ_1 and RIs in such a large RI range (Supplementary **Figure S7b**), which is more superior to that of conventional propagating surface plasmon based sensors.[23,24] Furthermore, although here we design and perform experimental demonstrations on PNRA sensor at visible frequency, its concept and sensing functionality can be easily extended to the infrared ranges by changing the structural parameters. It is notable that RI sensitivity of the PNRA sensor would increase for infrared operation frequency because the electromagnetic loss within metal layer is reduced at longer wavelength. For example, as shown in Supplementary **Figures S5a and S5b**. when the resonance wavelengths λ_1 is extended to the wavelength of 5000 nm, the RI sensitivity of resonance wavelengths λ_1 reaches up to 3800 nm RIU^{-1}. In addition, when the resonance wavelength λ_1 is adjusted from visible to infrared region, the

linewidth of the resonance spectrum almost keeps unchanged. Therefore, the FOM of the PNRA sensor can also be further increased at longer wavelength.

In summary, we demonstrate a PNRA device which can be used as a high-performance biosensing platform. The coupling of dipolar modes in nanohole and nanodisk arrays gives rise to a robust subradiant lattice plasmon resonance in the PNRA. The narrow spectral linewidth with high peak-to-dip signal ratio and strong near-field electromagnetic enhancement boost the refractive index sensitivity and FOM associated with the sensing device. In the experimental demonstrations, the PNRA not only realizes high sensitivity refractive index sensing, but also achieves real-time monitoring of biomolecular specific binding interactions at nanomolar concentrations. Compared with other plasmonic sensing devices, the PNRA does not require complicated angular illuminations and has polarization independent optical responses. Due to simple normal illumination and signal acquisition architecture, we transfer the PNRA onto the optical fiber tip and successfully achieve the integrated and remote biosensing. We envision the PNRA may be a potential candidate for developing a high performance photonic platform for point-of-care, label-free chemical and biomedical sensing.

METHOD

FDTD simulation. The simulations are performed based on the FDTD algorithm to obtain the reflectance spectra, electric field distribution and charge distribution of the PNRA at normal incidence. The periodic boundary conditions are applied in both *x* and *y* direction and perfectly matched layers are used in *z* direction. The grid size along the *x*, *y* and *z* direction is 2 nm × 2 nm × 2 nm, respectively. The dielectric permittivity of bulk gold in the visible and near-infrared

region is from Johnson and Christy.[57]

The preparation of plasmonic nanoring resonators array. First, a 3-nm Ti film and a 100-nm Au film are sputtered sequentially onto a 10 mm×10 mm quartz substrate and on the fine polishing end face of a 20-cm long optical fiber. The deposition rate for Ti and Au is $R_{Ti} \approx 0.016$ nm/s and $R_{Au} \approx 0.05$ nm/s, respectively. Then, subwavelength nanoring are fabricated by FIB milling using a dual-beam (FIB/SEM) system (Ga^+ ions, 24 pA beam current, 30k eV beam energy). The end face of optical fiber is polished in sequence using fiber optic polishing machine with 9 μm, 3 μm, 1 μm, 0.03 μm grit emery papers.

Q-factor extraction. We use an analytical model to extract the Q-factor of resonant dip in the PNRA. The calculated and measured spectra are fitted to an analytical model described by $R = |a_1 + ja_2 + b/(\omega - \omega_0 + j\gamma)|^2$, where the parameters a_1, a_2, and b are constant real numbers; the sign j stands for imaginary unit; ω_0 and γ refers to the center resonant frequency and overall damping rate of resonance.[58] The calculated and measured Q-factors are then determined by $Q = (\omega_0/2\gamma)$.

Measurements of reflectance spectra. For the structure with PNRA on the quartz substrate, a home-build Polydimethylsiloxane (PDMS) flow cell is employed as holders of liquids solution before optical measurement. The flow cell is sandwiched between the sensing substrate and a PMMA plate. Inlet and outlet holes are drilled through PMMA plate to connect the tubing. All reflectance spectra on the quartz substrate are taken on a UV-Visible-NIR micro-spectrometer (PV20/30 from CRAIC Technologies). For the structure with PNRA on the tip of optical fiber, a home-built flow cell is used for injection and the ejection of sample solutions and the sufficient space for washing sensing surfaces. Light source, spectrometer and the fiber probe are connected by a binary beam fiber jumper. Light from a halogen lamp (HL-2000-FHSA, Ocean Optics, Inc.) is launched into one splitter end of the fiber jumper. The transmission spectrum is collected at the other splitter end of the fiber jumper through the spectrometer (HR4000, Ocean Optics, Inc.) and is displayed by a computer. The probe is mounted in the

combined end of the fiber jumper. In the above optical measurement, a peristaltic pump is used to inject sample solutions with a constant flow rate of 0.2 ml/min.

Supporting Information

Supporting Information Available: The following files are available free of charge.

The results illustrating a broader line-shape in experiment; electric field distribution at resonant wavelengths for different structures; resonant wavelength and bulk refractive index sensitivity dependent on structure parameters; calculated reflectance spectra for different refractive index solutions; and figure of merit (FOM) of sensing detection.

ACKNOWLEDGMENTS

The work is supported in part by the Ministry of Science and Technology of China under Grant No. 2017YFA0303700, National Natural Science Foundation of China under Grant No. 61705100, 61575092, 61520106013. T. X. acknowledges support from the Thousand Talents Program for Young Professionals and Collaborative Innovations Center of Advanced Microstructures. W. Z. and A. A. acknowledge support under the Cooperative Research Agreement between the University of Maryland and the National Institute of Standards and Technology, Center for Nanoscale Science and Technology, Award#70NANB10H193, through the University of Maryland.

AUTHOR INFORMATION

Corresponding Author

***E-mail:** xuting@nju.edu.cn, yqlu@nju.edu.cn

ORCID

Yuzhang Liang: 0000-0002-6257-3547

Ting Xu: 0000-0002-0704-1089

Notes

The authors declare no competing financial interests.

REFERENCES

1. Anker, J. N.; Hall, W. P.; Lyandres, O.; Shah, N. C.; Zhao, J.; Van Duyne, R. P. Biosensing with plasmonic nanosensors. *Nat. Mater.* **2008**, 7, 442-453.
2. Mayer, K. M.; Hafner, J. H. Localized surface plasmon resonance sensors. *Che. Rev.* **2011**, 111, 3828-3857.
3. Yanik, A. A.; Huang, M.; Kamohara, O.; Artar, A.; Geisbert, T. W.; Connor, J. H.; Altug, H. An optofluidic nanoplasmonic biosensor for direct detection of live viruses from biological media. *Nano Lett.* **2010**, 10, 4962-4969.
4. Liu, N.; Mesch, M.; Weiss, T.; Hentschel, M.; Giessen, H. Infrared perfect absorber and its application as plasmonic sensor. *Nano Lett.* **2010**, 10, 2342-2348.
5. Zhang, S.; Bao, K.; Halas, N. J.; Xu, H.; Nordlander, P. Substrate-induced Fano resonances of a plasmonic nanocube: A route to increased-sensitivity localized surface plasmon resonance sensors revealed. *Nano Lett.* **2011**, 11, 1657-1663.
6. Verellen, N.; Van Dorpe, P.; Huang, C.; Lodewijks, K.; Vandenbosch, G. A. E.; Lagae, L.; Moshchalkov, V. V. Plasmon line shaping using nanocrosses for high sensitivity localized surface plasmon resonance sensing. *Nano Lett.* **2011**, 11, 391-397.
7. Schmidt, M. A.; Lei, D. Y.; Wondraczek, L.; Nazabal, V.; Maier, S. A. Hybrid nanoparticle-microcavity-based plasmonic nanosensors with improved detection resolution and extended remote-sensing ability. *Nat. Commun.* **2012**, 3, 1108.
8. Wu, C. H.; Khanikaev, A. B.; Adato, R.; Arju, N.; Yanik, A. A.; Altug, H.; Shvets, G. Fano-resonant asymmetric metamaterials for ultrasensitive spectroscopy and identification of molecular monolayers. *Nat. Mater.* **2012**, 11, 69-75.
9. Shen, Y.; Zhou, J. H.; Liu, T. R.; Tao, Y. T.; Jiang, R. B.; Liu, M. X.; Xiao, G. H.; Zhu, J. H.; Zhou, Z. K.; Wang, X. H.; Jin, C. J.; Wang, J. F. Plasmonic gold mushroom arrays with refractive index sensing figures of merit approaching the theoretical limit. *Nat. Commun.* **2013**, 4, 2381.
10. Li, N.; Tittl, A.; Yue, S.; Giessen, H.; Song, C.; Ding, B.; Liu, N. DNA-assembled bimetallic plasmonic nanosensors. *Light: Sci. Appl.* **2014**, 3, e226.
11. Feng, J.; Pacifici, D. A spectroscopic refractometer based on plasmonic interferometry. *J. Appl. Phys.* **2016**, 119, 083104.

12. Li, D.; Feng, J.; Pacifici, D. Nanoscale optical interferometry with incoherent light. *Sci. Rep.* **2016**, 6, 20836.
13. Hui, Y.; Gomez-Diaz, J. S.; Qian Z.; Andrea A.; Rinaldi, M. Plasmonic piezoelectric nanomechanical resonator for spectrally selective infrared sensing, *Nat. Commun.* **2016**, 7, 11249.
14. Zhao, Y.; Askarpour, A. N.; Sun, L.; Shi, J.; Li, X.; Andrea A. Chirality detection of enantiomers using twisted optical metamaterials, *Nat. Commun.* **2017**, 8, 14180.
15. Yuan, J.; Duan, R.; Yang, H.; Luo, X.; Xi, M. Detection of serum human epididymis secretory protein 4 in patients with ovarian cancer using a label-free biosensor based on localized surface plasmon resonance. *Int. J. Nanomed.* **2012**, 7, 2921-2928.
16. Zhang, K.; Zhang, L.; Yap, F. L.; Song, P.; Qiu, C. W.; Loh, K. P. Large-area graphene nanodot array for plasmon-enhanced infrared spectroscopy. *Small* **2016**, 12, 1302-1308.
17. Peng, L.; Zhang, L.; Yuan, J.; Chen, C.; Bao, Q.; Qiu, C. W.; Peng Z.; Zhang, K. Gold nanoparticle mediated graphene plasmon for broadband enhanced infrared spectroscopy. *Nanotechnology* **2017**, 28, 264001.
18. Yuan, Y. J.; Jia, R. Study on pivot-point vibration of molecular bond-rupture events by quartz crystal microbalance for biomedical diagnostics. *Int. J. Nanomed.* **2012**, 7, 381-391.
19. Feng, J.; Li, D.; Pacifici, D. Circular slit-groove plasmonic interferometers: a generalized approach to high-throughput biochemical sensing. *Opt. Mater. Express* **2015**, 5, 2742-2753.
20. Siu, V. S.; Feng, J.; Flanigan, P. W.; Palmore, G. T. R.; Pacifici, D. A “plasmonic cuvette”: dye chemistry coupled to plasmonic interferometry for glucose sensing. *Nanophotonics* **2014**, 3, 125-140.
21. Feng, J.; Siu, V. S.; Roelke, A.; Mehta, V.; Rhieu, S. Y.; Palmore, G. T. R.; Pacifici, D. Nanoscale plasmonic interferometers for multispectral, high-throughput biochemical sensing. *Nano Lett.* **2012**, 12, 602-609.
22. Rothenhäuslar, B.; Knoll, W. Surface-plasmon microscopy. *Nature* **1988**, 332, 615-617.
23. Homola, J.; Yee, S. S.; Gauglitz, G. Surface plasmon resonance sensors: Review. *Sens. Actuators B: Chem.* **1999**, 54, 3-15.
24. Homola, J. Surface plasmon resonance sensors for detection of chemical and biological species. *Chem. Rev.* **2008**, 108, 462-493.

25. Luppa, P. B.; Müller, C.; Schlichtiger, A.; Schlebusch, H. Point-of-care testing (POCT): Current techniques and future perspectives. *Trends Anal. Chem.* **2011**, 30, 887-898.
26. Jensen, T. R.; Malinsky, M. D.; Haynes, C. L.; Van Duyne, R. P. Nanosphere lithography: tunable localized surface plasmon resonance spectra of silver nanoparticles. *J. Phys. Chem. B* **2000**, 104, 10549-10556.
27. Malinsky, M. D.; Kelly, K. L.; Schatz, G. C.; Van Duyne, R. P. Chain length dependence and sensing capabilities of the localized surface plasmon resonance of silver nanoparticles chemically modified with alkanethiol self-assembled monolayers. *J. Am. Chem. Soc.* **2001**, 123, 1471-1482.
28. Hao, F.; Sonnefraud, Y.; Van Dorpe, P.; Maier, S. A.; Halas, N. J.; Nordlander, P. Symmetry breaking in plasmonic nanocavities: Subradiant LSPR sensing and a tunable Fano resonance. *Nano Lett.* **2008**, 8, 3983-3988.
29. Sonnefraud, Y.; Verellen, N.; Sobhani, H.; Vandenbosch, G. A. E.; Moshchalkov, V. V.; Van Dorpe, P.; Nordlander, P.; Maier, S. A. Experimental realization of subradiant, superradiant, and Fano resonances in Ring/Disk plasmonic nanocavities. *ACS Nano* **2010**, 4, 1664-1670.
30. Cetin, A. E.; Altug, H. Fano resonant ring/disk plasmonic nanocavities on conducting substrates for advanced biosensing. *ACS Nano* **2012**, 6, 9989-9995.
31. Fan, J. A.; Wu, C.; Bao, K.; Bao, J.; Bardhan, R.; Halas, N. J.; Manoharan, V. N.; Nordlander, P.; Shvets, G.; Capasso, F. Self-assembled plasmonic nanoparticle clusters. *Science* **2010**, 328, 1135-1138.
32. Lassiter, J. B.; Sobhani, H.; Fan, J. A.; Kundu, J.; Capasso, F.; Nordlander, P.; Halas, N. J. Fano resonances in plasmonic nanoclusters: geometrical and chemical tunability. *Nano Lett.* **2010**, 10, 3184-3189.
33. Alonso-Gonzalez, P.; Schnell, M.; Sarriugarte, P.; Sobhani, H.; Wu, C.; Arju, N.; Khanikaev, A.; Golmar, F.; Albella, P.; Arzubiaga, L.; Casanova, F.; Hueso, L. E.; Nordlander, P.; Shvets, G.; Hillenbrand, R. Real-space mapping of Fano interference in plasmonic metamolecules. *Nano Lett.* **2011**, 11, 3922-3926.
34. König, M.; Rahmani, M.; Zhang, L.; Lei, D. Y.; Roschuk, T. R.; Giannini, V.; Qiu, C. W.; Hong M. H.; Schlücker S.; Maier, S. A. Unveiling the correlation between nanometer-thick

molecular monolayer sensitivity and near-field enhancement and localization in coupled plasmonic oligomers. *ACS Nano* **2014**, 8, 9188-9198.

35. Zou, S. L.; Janel, N.; Schatz, G. C. Silver nanoparticle array structures that produce remarkably narrow plasmon lineshapes. *J. Chem. Phys.* **2004**, 120, 10871-10875.
36. Auguie, B.; Barnes, W. L. Collective resonances in gold nanoparticle arrays. *Phys. Rev. Lett.* **2008**, 101, 143902.
37. Vecchi, G.; Giannini, V.; Rivs, J. G. Shaping the fluorescent emission by lattice resonances in plasmonic crystals of nanoantennas. *Phys. Rev. Lett.* **2009**, 102, 146807.
38. Zhou, W.; Odom, T. W. Tuanable subradiant lattice plasmons by out-of-plane dipolar interactions, *Nat. Nanotech.* **2011**, 6, 423-427.
39. Kabashin, A. V.; Evans, P.; Pastkovsky, S.; Hendren, W.; Wurtz, G. A.; Atkinson, R.; Pollard, R.; Podolskiy, V. A.; Zayats, A. V. Plasmonic nanorod metamaterials for biosensing. *Nat. Mater.* **2009**, 8, 867-871.
40. Sreekanth, K. V.; Alapan, Y.; ElKabbash, M.; Ilker, E.; Hinczewski, M.; Gurkan, U. A.; De Luca, A.; Strangi, G. Extreme sensitivity biosensing platform based on hyperbolic metamaterials. *Nat. Mater.* **2016**, 15, 621-627.
41. Luk'yanchuk, B.; Zheludev, N. I.; Maier, S. A.; Halas, N. J.; Nordlander, P.; Giessen, H.; Chong, C. T. The Fano resonance in plasmonic nanostructures and metamaterials. *Nat. Mater.* **2010**, 9, 707-715.
42. Miroshnichenko, A. E.; Flach, S.; Kivshar, Y. S. Fano resonances in nanoscale structures. *Rev. Mod. Phys.* **2010**, 82, 2257-2298.
43. Hao, F.; Nordlander, P.; Sonnefraud, Y.; Van Dorpe, P.; Maier, S. A. Tunability of subradiant dipolar and Fano-type plasmon resonances in metallic ring/disk cavities: Implications for nanoscale optical sensing. *ACS Nano* **2009**, 3, 643-652.
44. Consales, M.; Ricciardi, A.; Crescitelli, A.; Esposito, E.; Cutolo, A.; Cusano, A. Lab-on-fiber technology: Toward multifunctional optical nanoprobes. *ACS Nano* **2012**, 6, 3163-3170.
45. Ricciardi, A.; Crescitelli, A.; Vaiano, P.; Quero, G.; Consales, M.; Pisco, M.; Esposito, E.; Cusano, A. Lab-on-fiber technology: a new vision for chemical and biological sensing. *Analyst* **2015**, 140, 8068-8079.

46. Kostovski, G.; Stoddart, P. R.; Mitchell, A. The optical fiber tip: An inherently light-coupled microscopic platform for micro- and nanotechnologies. *Adv. Mater.* **2014**, 26, 3798-3820.
47. Cusano, A.; Consales, M.; Crescitelli, A.; Ricciardi, A. *Lab-On-Fiber Technology*. (Springer, 2015).
48. Morrill, D.; Li, D.; Pacifici, D. Measuring subwavelength spatial coherence with plasmonic interferometry. *Nat. Photon.* **2016**, 10, 681-687.
49. Li, D.; Feng, J.; Pacifici, D. Higher-order surface plasmon contributions to passive and active plasmonic interferometry. *Opt. Express* **2016**, 24, 27309-27318.
50. Prodan, E.; Radloff, C.; Halas, N. J.; Nordlander, P. A hybridization model for the plasmon response of complex nanostructures. *Science* **2003**, 302(5644), 419-422.
51. Clausen, J. S.; Hojlund-Nielsen, E.; Christiansen, A. B.; Yazdi, S.; Grajower, M.; Taha, H.; Levy, U.; Kristensen, A.; Mortensen, N. A. Plasmonic metasurfaces for coloration of plastic consumer products. *Nano Lett.* **2014**, 14, 4499-4504.
52. Verellen, N.; Sonnefraud, Y.; Sobhani, H.; Hao, F.; Moshchalkov, V. V.; Dorpe, P. V.; Nordlander P.; Maier, S. A. Fano resonances in individual coherent plasmonic nanocavities. *Nano Lett.* **2009**, 9, 1663-1667.
53. Zhang, L.; Dong, Z.; Wang, Y. M.; Liu, Y. J.; Zhang, S.; Yang, J. K. W.; Qiu, C. W. Dynamically configurable hybridization of plasmon modes in nanoring dimer arrays. *Nanoscale* **2015**, 7, 12018-12022.
54. Liu, Y.; Liu, Q.; Chen, S.; Cheng, F.; Wang, H.; Peng, W. Surface plasmon resonance biosensor based on smart phone platforms. *Sci. Rep.* **2015**, 5, 12864.
55. Cheng, F.; Shang, J.; Ratner, D. M. A versatile method for functionalizing surfaces with bioactive glycans. *Bioconjugate. Chem.* **2011**, 22, 50-57.
56. Liu, Y.; Chen, S.; Liu, Q.; Masson, J.-F.; Peng, W. Compact multi-channel surface plasmon resonance sensor for real-time multi-analyte biosensing. *Opt. Express* **2015**, 23, 20540-20548.
57. Johnson, P. B.; Christy, R. W. Optical constants of noble metals. *Phys. Rev. B* **1972**, 6, 4370-4379.
58. Yang, Y.; Kravchenko, I. I.; Briggs, D. P.; Valentine, J. All-dielectric metasurface analogue

of electromagnetically induced transparency. *Nat. Commun.* **2014**, 5, 5753.

Figure and caption

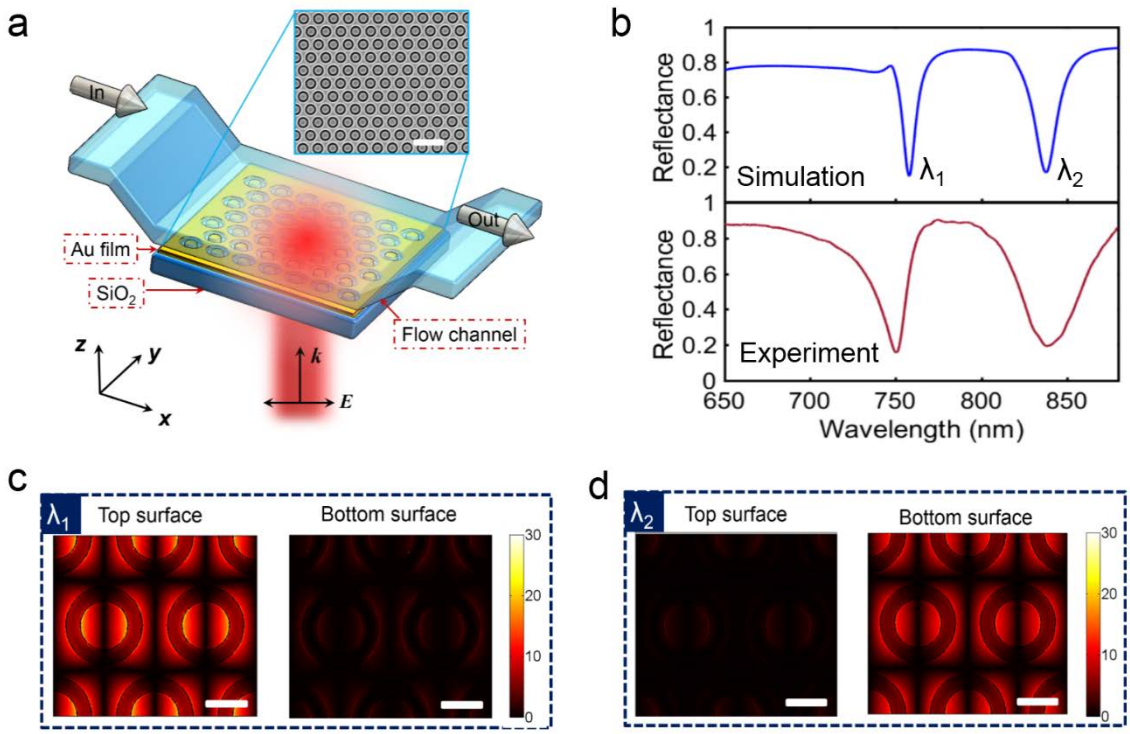

Figure 1. Geometry and optical characteristics of Au PNRA. (a) Schematic representation of the fabricated miniaturized PNRA sensor device with a fluid flow channel and a top-down scanning electron microscopy image of the fabricated PNRA (Scale bar, 2 μm). The periodicity (*P*) of the PNRA is 640 nm and the thickness of the Au film is 100 nm. The inner radius (*r*) and outer radius (*R*) of the nanoring are 150 nm and 240 nm, respectively. (b) The theoretical (blue solid line: FDTD simulation) and experimental (red solid line) reflectance spectra. Electric field |*E*| distribution on the top and bottom surfaces of nanoring array at resonant wavelengths (c) λ_1 and (d) λ_2. Scale bar, 300 nm.

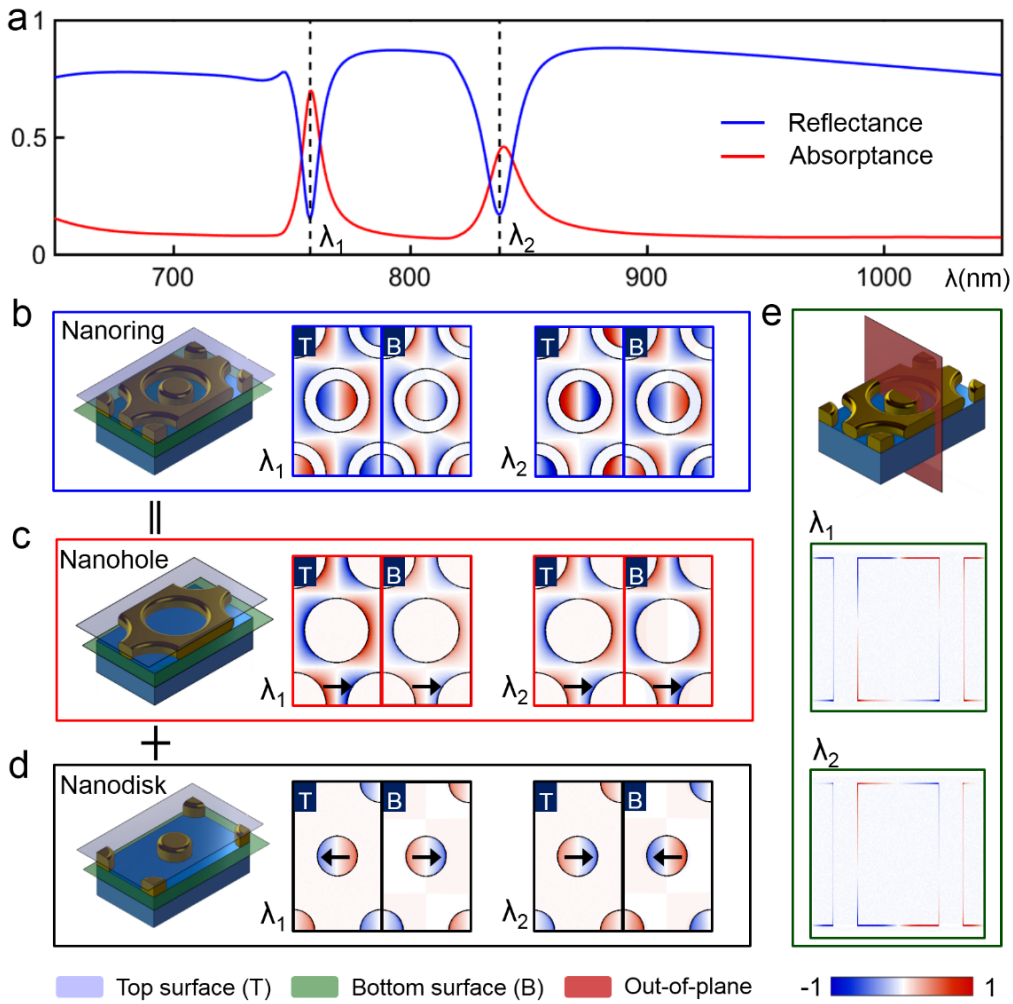

Figure 2. Dipolar interactions in the PNRA. (a) The calculated reflectance (absorptance) spectrum of the PNRA with periodicity P = 640 nm, inner radius r = 150 nm, outer radius D = 240 nm and Au film thickness 100 nm. The calculated in-plane normalized surface charge distributions of the relevant modes at both top and bottom surfaces of (b) nanoring, (c) nanhole and (d) nanodisk arrays at resonant wavelengths λ_1 and λ_2, where the directions of dipolar modes are indicated by the black arrows. (e) The calculated out-of-plane normalized surface charge distributions of PNRA at resonant wavelengths λ_1 and λ_2. The top and bottom surfaces and out-of-plane are indicated by blue, green and red planes, respectively. To clearly exhibit out-of-plane normalized surface charge distributions, Fig. 2e is plotted out-of-scale compared to the actual structure size.

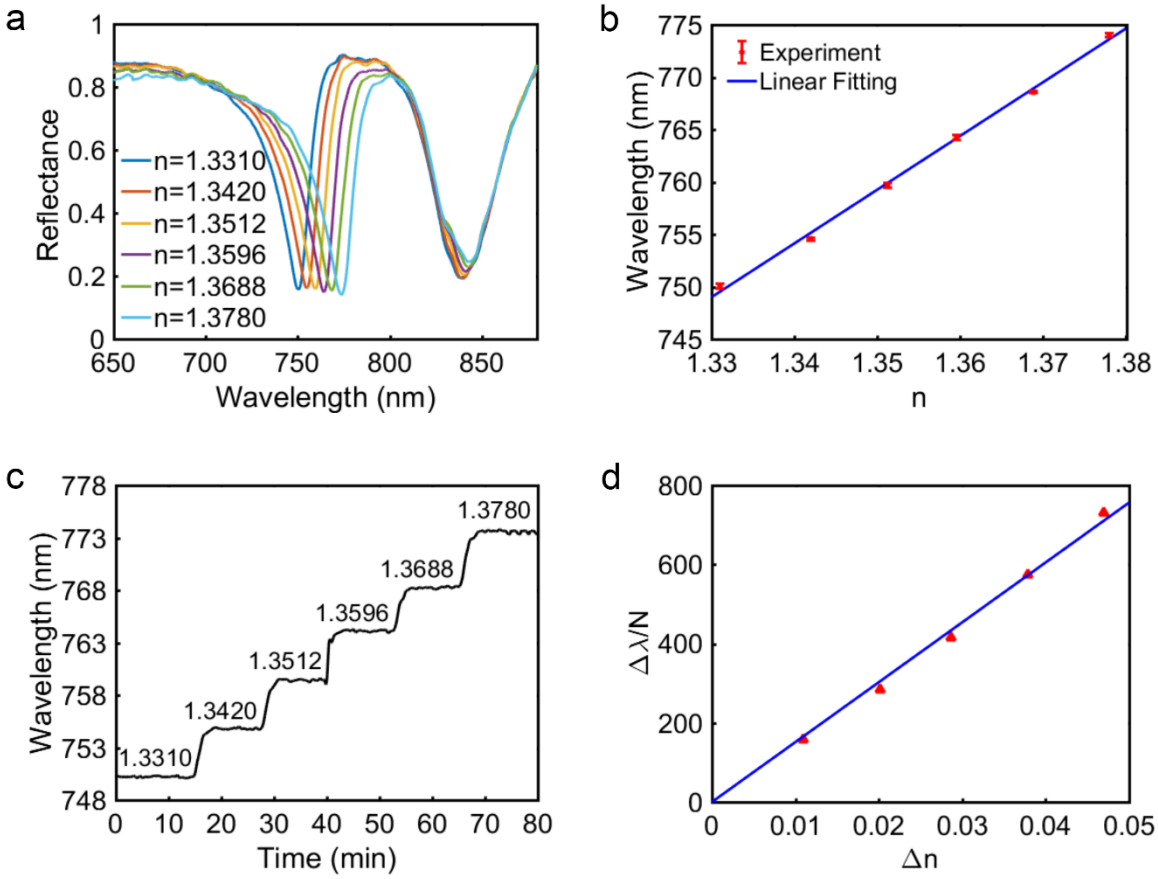

Figure 3. Evaluation of PNRA sensor device integrated with microfluidics. (a) Measured reflectance spectra of the sensor device for different refractive index of sodium chloride solutions. (b) Relationship between experimentally measured resonance dip position and the refractive index. Uncertainties in (b) are based on the standard deviations of five repeated measurements for every experimental data point. The upper and lower limits of the error bar in (b) are too small to be clearly seen. (c) Wavelength shifts of dip for different refractive index of sodium chloride solutions as a function of time. (d) The relationship between wavelength shifts normalized experiment noise (*N*) and refractive index change in order to evaluate the limit of detection for a PNRA.

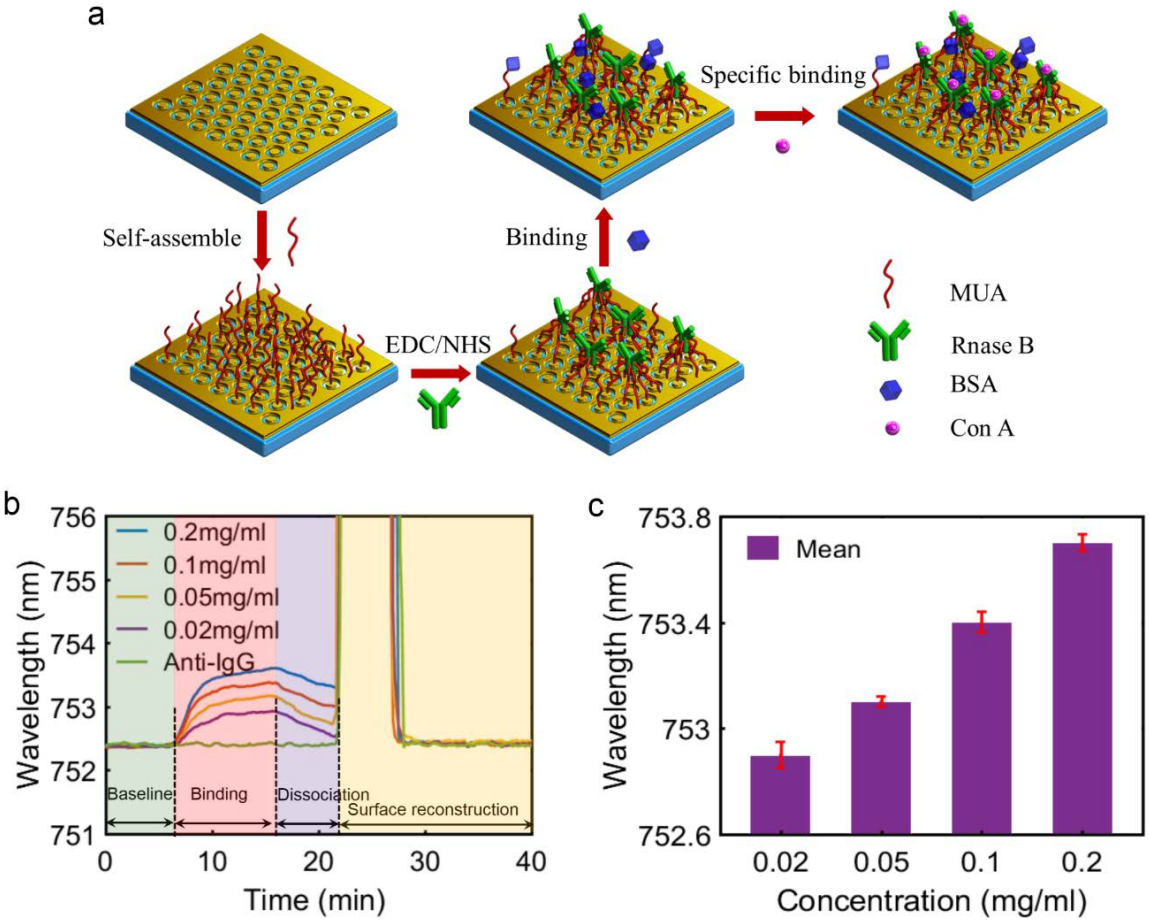

Figure 4. The PNRA as a label-free biosensor to detect protein biomolecule. (a) The experiment detection flow-chart for the specific binding of Con A and Rnase B. (b) Real-time biomolecular interaction response for the detection of Con A at the concentrations of 0.02 mg/ml, 0.05 mg/ml, 0.1 mg/ml and 0.2 mg/ml. The turquoise line shows the nonspecific binding of Rnase B and anti-IgG of 0.1 mg/ml. (c) The relationship between the measured wavelength positions and Con A concentration. Each measurement at a given concentration is repeated three times. The mean and standard deviation are calculated.

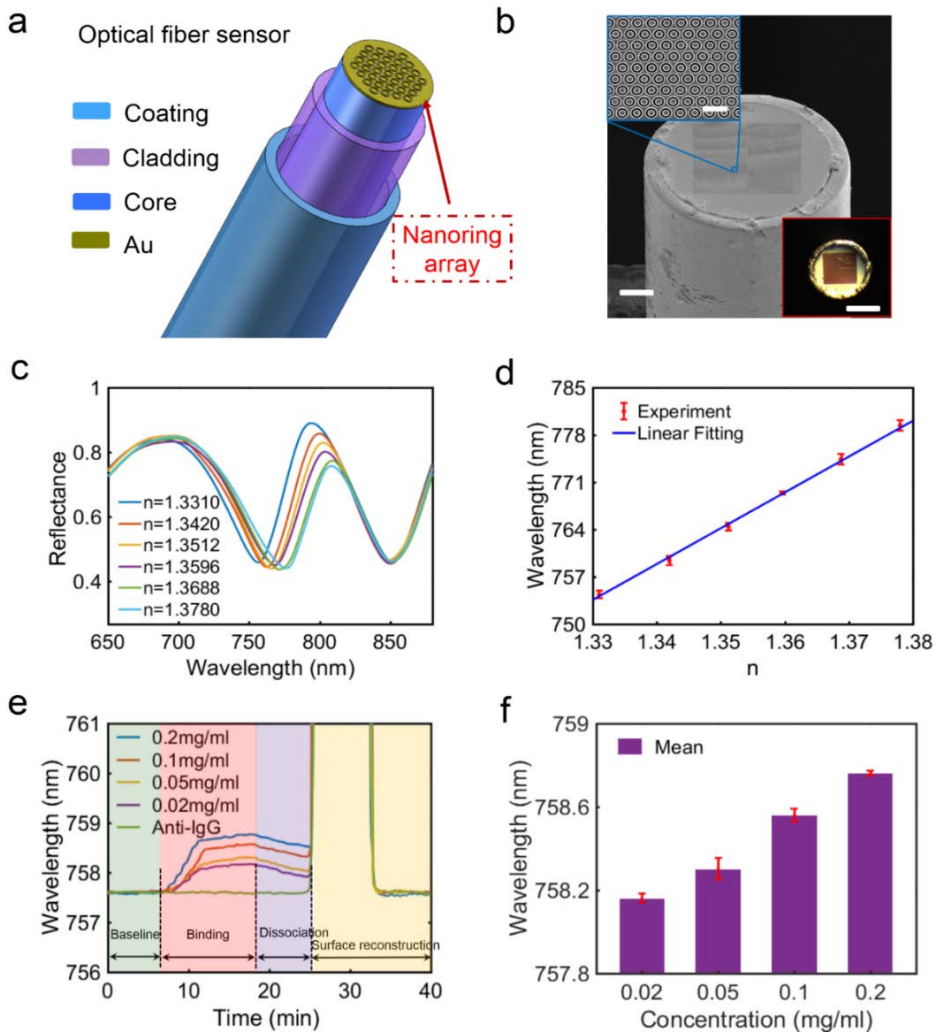

Figure 5. The PNRA integrated with the optical fiber for remote biosensing. (a) Schematic representation of the optical fiber sensor device with PNRA integrated on the end face of optical fiber. (b) Oblique-view SEM images of the fabricated PNRA on the optical fiber end face. Scale bar, 50 μm. Inset at left corner is magnified SEM image. Scale bar, 1 μm. Inset at right corner is microscope image. Scale bar, 150 μm. (c) Experimentally measured reflectance spectra of the optical fiber sensor device for various refractive index of NaCl solutions. (d) Relationship between measured resonance dip position and the refractive index. Uncertainties are based on the standard deviations of five repeated measurements for every experimental data point. (e) Real-time specific detection of optical fiber sensor device for different concentrations of Con A. The turquoise line shows the nonspecific binding of Rnase B and anti-IgG of 0.1 mg/ml. (f) The relationship between the measured wavelength position and Con A concentration. Each measurement at a given concentration is repeated three times.

For TOC only

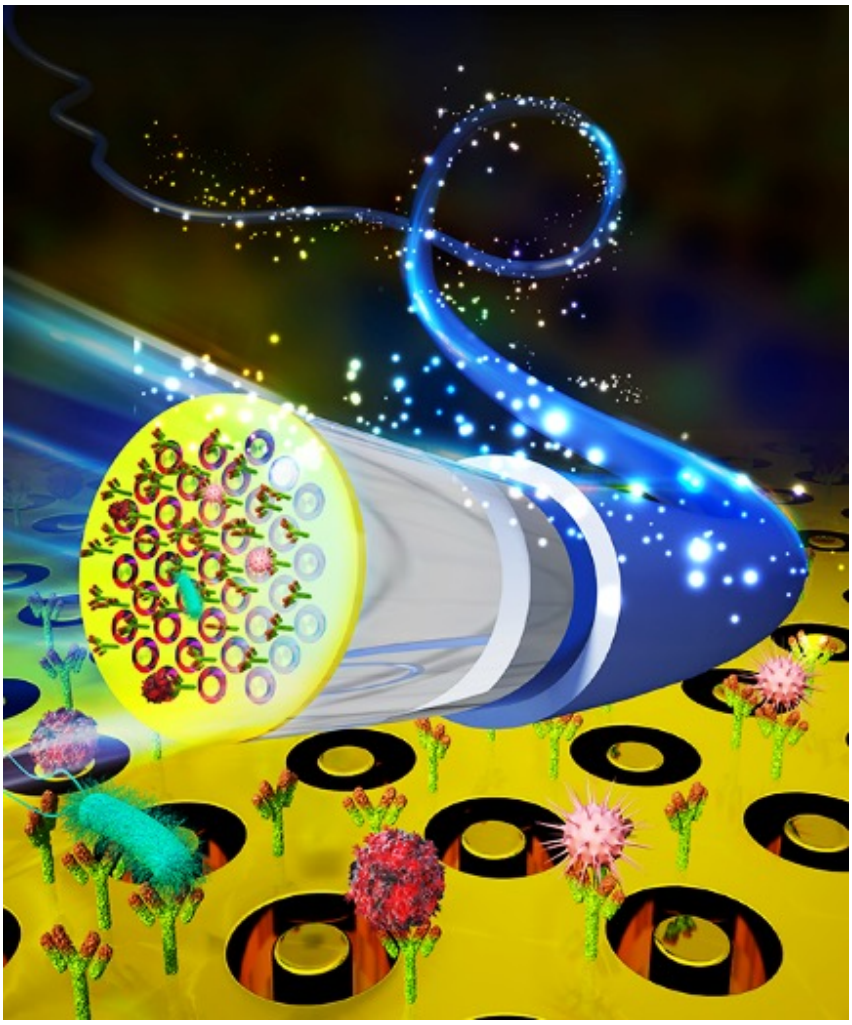

Supporting information

Subradiant dipolar interactions in plasmonic nanoring resonator array for integrated label-free biosensing

Yuzhang Liang[1], Hui Zhang[1], Wenqi Zhu[2,3], Amit Agrawal[2,3], Henri Lezec[2], Lixia Li[4], Wei Peng[4], Yi Zou[1], Yanqing Lu[1] and Ting Xu[1,*]

[1] National Laboratory of Solid State Microstructures, College of Engineering and Applied Sciences, Collaborative Innovation Center of Advanced Microstructures, Nanjing University, Nanjing 210093, China.

[2] Center for Nanoscale Science and Technology, National Institute of Standards and Technology, Gaithersburg, MD 20899, USA.

[3] Maryland NanoCenter, University of Maryland, College Park, MD 20742, USA.

[4] College of Physics and Optoelectronics Engineering, Dalian University of Technology, Dalian 116024, China.

[*] Email: xuting@nju.edu.cn, yqlu@nju.edu.cn

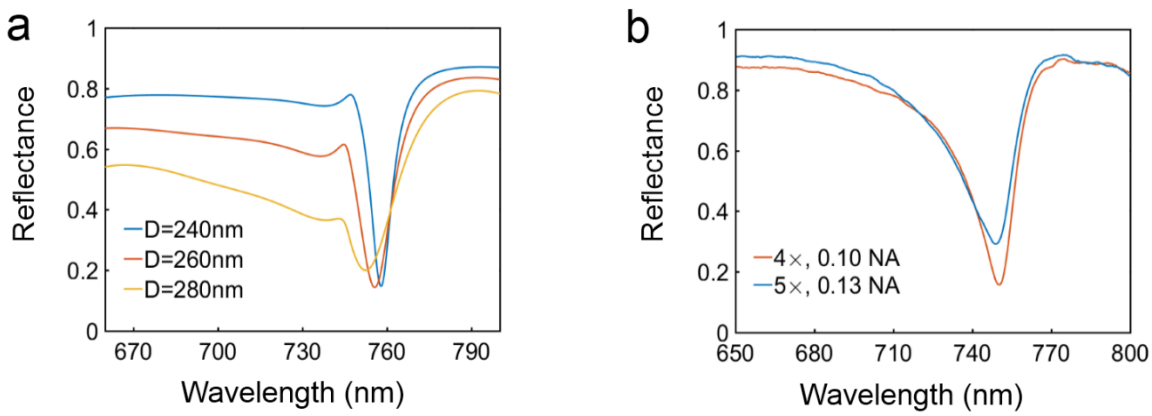

Figure S1 (a) The influence of outer radius (*D*) on the line-shape of resonance dip λ_1. It can be clearly seen that the line width of resonant wavelength λ_1 increases and the peak-to-dip signal ratio decreases with the increase of outer radius. (b) Comparison of the measured reflectance spectra with different numerical aperture and amplification of objective lens. We can see that resonant dip λ_1 has a narrow line-shape with low numerical aperture objective lens used.

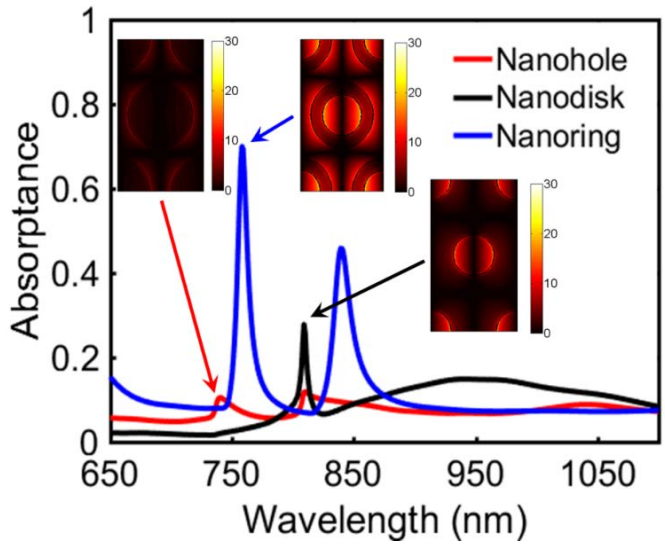

Figure S2. Calculated absorptance spectra for nanohole, nanodisk and nanoring and corresponding electric field distributions on the top surface at their resonant wavelengths. The narrow-band absorptance reaches to 0.7 at the wavelength of 758 nm in the nanoring array, which is higher than that of nanohole and nanodisk array. Moreover, electric field distribution of nanoring structure is also much stronger than those of pure nanohole and nanodisk structures at the resonant wavelength.

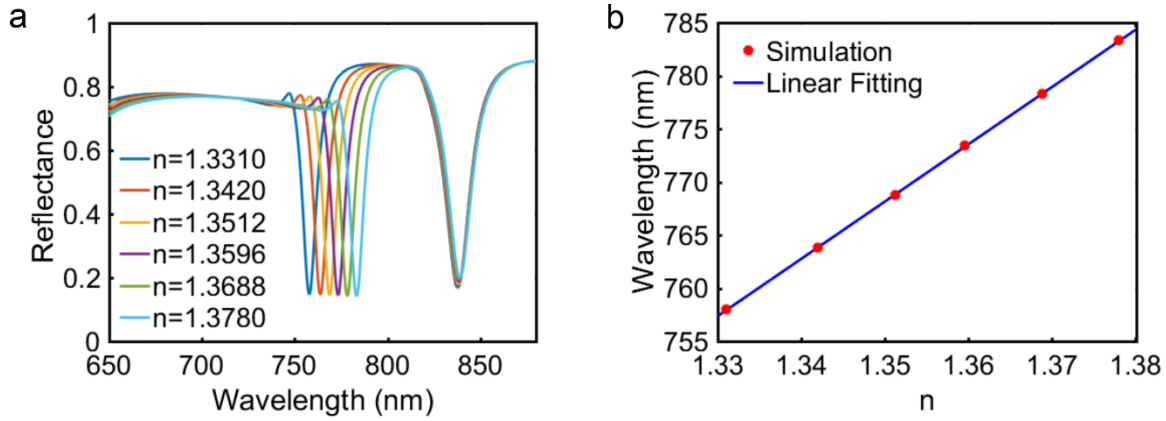

Figure S3. (a) Calculated reflectance spectra of the sensor device for different refractive index of sodium chloride solutions. (b) Relationship between calculated resonance dip position and the refractive index.

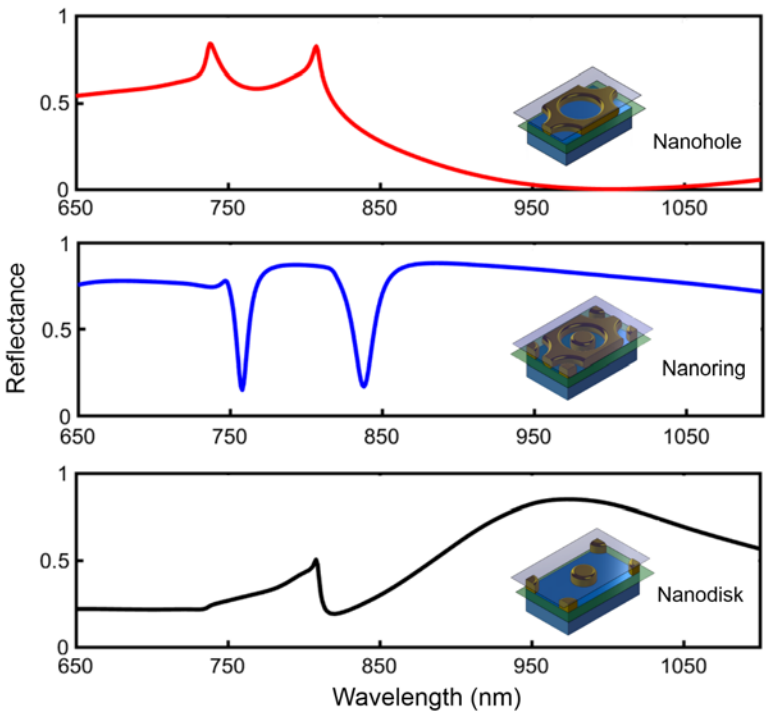

Figure S4. Calculated reflectance spectra for nanohole, nanodisk and nanoring array structures. Compared to that of nanohole and nanodisk structures, the nanoring array has narrower line-shape and high peak-to-dip signal ratio.

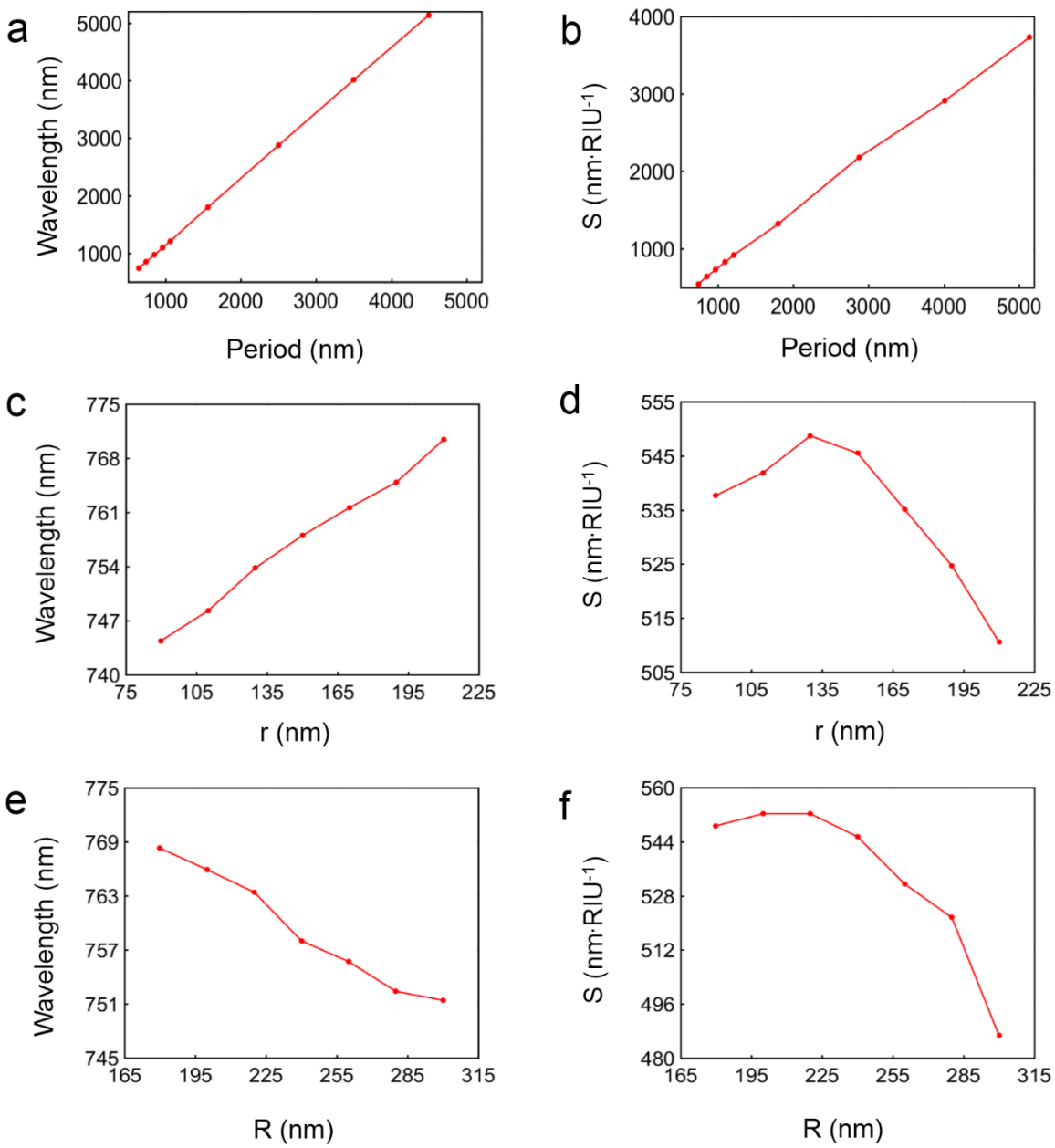

Figure S5. The influence of structure periodicity *P* on (a) resonant wavelength λ_1 and (b) bulk refractive index sensitivity. The influence of inner radius *r* on (c) resonant wavelength λ_1 and (d) bulk refractive index sensitivity. The influence of outer radius *R* on (e) resonant wavelength λ_1 and (f) bulk refractive index sensitivity.

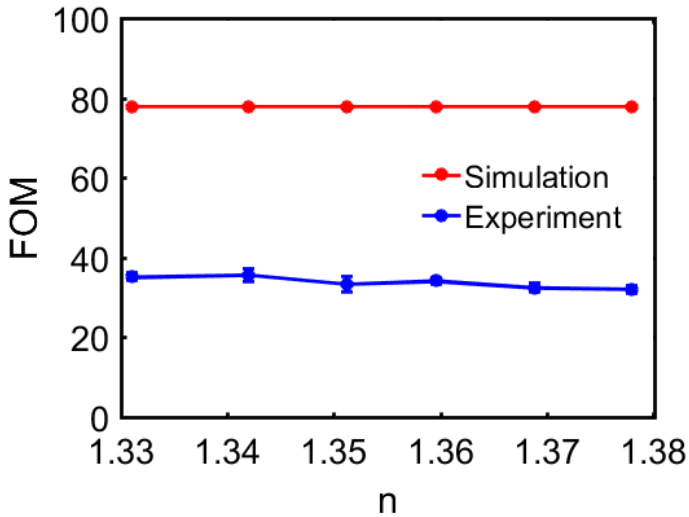

Figure S6. The measured FOM and simulated FOM of resonant dip for different RI solutions. The simulated FOM values of resonant dip (~78 RIU^{-1}) are two-fold higher than that in experiment (~35 RIU^{-1}). Uncertainties are based on the standard deviations of five repeated measurements for every experimental data point.

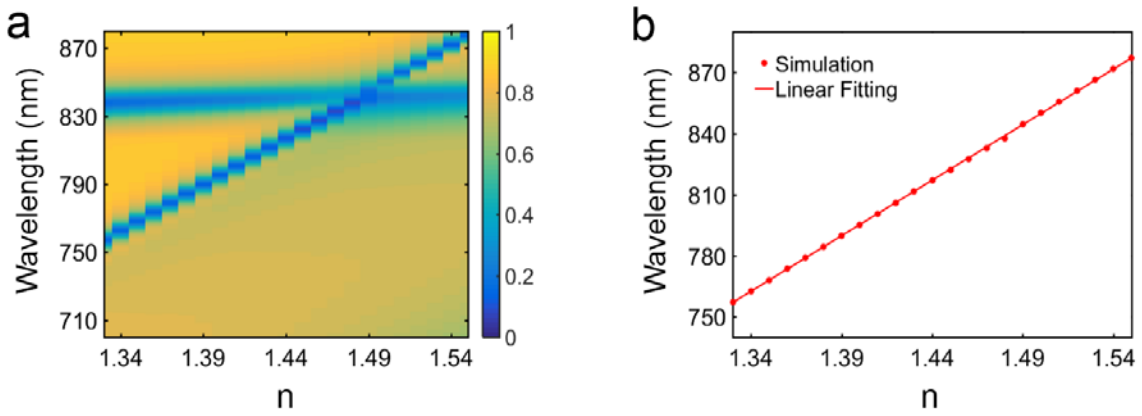

Figure S7. (a) Calculated reflectance spectra of the PNRA with the refractive index range from 1.33 to 1.55. (b) Relationship between calculated resonance wavelength λ_1 and the refractive index at the top surface of the plasmonic nanoring array structure.